

# Noninvasive Optical Tracking of Red Fluorescent Protein–Expressing Cancer Cells in a Model of Metastatic Breast Cancer<sup>1\*</sup>

Paul T. Winnard Jr., Jessica B. Kluth and Venu Raman

Department of Radiology, The Johns Hopkins University School of Medicine, Baltimore, MD 21205, USA

## Abstract

We have evaluated the use of the Xenogen IVIS 200 imaging system for real-time fluorescence protein–based optical imaging of metastatic progression in live animals. We found that green fluorescent protein–expressing cells ( $100 \times 10^6$ ) were not detectable in a mouse cadaver phantom experiment. However, a 10-fold lower number of tdTomato-expressing cells were easily detected. Mammary fat pad xenografts of stable MDA-MB-231-tdTomato cells were generated for the imaging of metastatic progression. At 2 weeks postinjection, barely palpable tumor burdens were easily detected at the sites of injection. At 8 weeks, a small contralateral mammary fat pad metastasis was imaged and, by 13 weeks, metastases to lymph nodes were detectable. Metastases with nodular composition were detectable within the rib cage region at 15 weeks. 3-D image reconstructions indicated that the detection of fluorescence extended to approximately 1 cm below the surface. A combination of intense tdTomato fluorescence, imaging at  $\geq 620$  nm (where autofluorescence is minimized), and the sensitivity of the Xenogen imager made this possible. This study demonstrates the utility of the noninvasive optical tracking of cancer cells during metastatic progression with endogenously expressed fluorescence protein reporters using detection wavelengths of  $\geq 620$  nm.

*Neoplasia* (2006) 8, 796–806

**Keywords:** Breast cancer, optical imaging, tdTomato, Xenogen, metastasis.

## Introduction

Modeling human disease states in mice has a profound impact on our understanding of disease progression and treatment development. The need for the noninvasive longitudinal monitoring of such model systems has resulted in the development of small animal imaging technologies such as micro–computed tomography, micro–positron emission tomography, magnetic resonance imaging, and optical imaging, all of which are now capable of providing real-time images of disease states [2]. Such imaging capabilities have provided the means for obtaining crucial information, such as the migration of cells to different parts of an

embryo during development [3], the fate of stem cells injected for therapeutic purposes [4], and the course of metastatic progression [5,6]. Combining imaging modalities usually provides critical information that might not be possible with the use of a single modality [2]. Toward this goal, we have developed and validated an optical fluorescence imaging method that can be combined with other imaging modalities.

Here, we report the first-time use of an orange-red fluorescent protein (tdTomato) [1] as reporter for the real-time optical imaging of breast cancer metastatic progression. We have demonstrated the feasibility of tracking metastases into the lung region of severe combined immunodeficient (SCID) mice with minimal autofluorescence by using the highly sensitive Xenogen IVIS 200 System (Xenogen system; Xenogen Corp., Alameda, CA) [7] and detection wavelengths at and above 620 nm.

## Materials and Methods

### *Mammalian Expression Vector Preparations, Transfections, and Stable Clone Selection*

The coding sequences of mCherry, mPlum, and tdTomato were kindly supplied by Roger Tsien as plasmids: pRSET<sub>B</sub>-mCherry, pBAD-mPlum, and pRSET<sub>B</sub>-tdTomato. The coding sequence of the green fluorescent protein (GFP) was from pEGFP N1 (Clontech Laboratories, Inc., Mountain View, CA). All four coding sequences were cloned into the mammalian expression vector pEF-1 $\alpha$ -myc/his (Invitrogen, Carlsbad, CA).

MCF-7 breast cancer cells were maintained in Eagle's minimal essential medium supplemented with 10% fetal bovine serum (FBS), whereas MDA-MB-231 breast cancer cells were grown in RPMI with the same supplement.

Abbreviations: FACS, fluorescence-activated cell sorting; SCID, severe combined immunodeficient

Address all correspondence to: Venu Raman, Department of Radiology, The Johns Hopkins University School of Medicine, 340 Traylor Building, 720 Rutland Avenue, Baltimore, MD 21205. E-mail: vraman2@jhmi.edu

<sup>1</sup>This work was supported by National Institutes of Health grant P50 CA103175.

\*This article refers to a supplementary material, which is designated by "W" (i.e., Figure W1) and is available online at [www.bcdecker.com](http://www.bcdecker.com).

Received 19 April 2006; Revised 8 August 2006; Accepted 11 August 2006.

Copyright © 2006 Neoplasia Press, Inc. All rights reserved 1522-8002/06/\$25.00  
DOI 10.1593/neo.06304

Transient transfections were performed with the TransIT-LT1 transfection reagent (Mirus Bio Corp., Madison, WI), according to the manufacturer's protocol. Briefly,  $2.5 \times 10^5$  MCF-7 cells were transfected with 2  $\mu\text{g}$  of plasmid DNA. Following transfections, the plates were incubated overnight (16–18 hours), and the medium was changed before analyses.

For stable transfections, MDA-MB-231 cells ( $1 \times 10^6$ ) were transfected with 2  $\mu\text{g}$  of pEF-1 $\alpha$ -tdTomato using Amaxa Nucleofector II instrument (Amaxa Biosystems, Gaithersburg, MD), according to its manual. Three weeks following the expansion of fluorescent cells, fluorescence-activated cell sorting (FACS) was performed at The Johns Hopkins University Flow Cytometry Core Facility using a FACS Vantage SE (Becton Dickinson, Franklin Lakes, NJ) instrument. Gating was performed on the brightest cells, which were collected and subsequently expanded without any antibiotic selection. Stable clones of MDA-MB-231-expressing GFP (MDA-MB-231-GFP) were a kind gift from Dr. LuZhe Sun (UT Health Science Center at San Antonio, San Antonio, TX) and were maintained in McCoy's medium supplemented with 10% FBS.

#### Mouse Cadaver Phantom

Stable MDA-MB-231-tdTomato and MDA-MB-231-GFP cells were lifted off plastic flasks with 10 mM EDTA in Hank's buffered saline. Cells were counted, centrifuged at 500g, and suspended in sterile phosphate-buffered saline (PBS). The desired number of cells ( $100 \times 10^6$ ) was then centrifuged at 700g and packed into small ( $\sim 6 \times 7$ –8 mm) cylindrical glass tubes that were sealed with parafilm at each end (Figure 2). During the course of the experiment, lower numbers of MDA-MB-231-tdTomato cells ( $45 \times 10^6$  and  $9.25 \times 10^6$ ) or MDA-MB-231-GFP cells ( $100 \times 10^6$ ) were placed into smaller tapered tubes and sealed with parafilm (Figure 2). All tubes were constructed from the bulb end or the center region of pasture pipettes using a glass cutter.

A SCID mouse was sacrificed according to National Institutes of Health and institutional guidelines. The skin on the dorsal side of the mouse was peeled back from both sides of the spinal column. Incisions that cut through the ribs were made along both sides of the spinal column, starting from the neck region and extending through the length of the rib cage (i.e., the lung/heart cavity). The muscle wall at the level of the diaphragm was cut from the spinal column down to the level of the side of the animal on both sides. A similar set of incisions was made near the neck, and muscle/rib flaps were pulled open. The lungs and the heart were moved upward and outward while simultaneously inserting the red and green fluorescent tubes into the opposite sides of the chest cavity, which placed the tubes directly against the inside of the ventral rib cage. This allowed the tubes to be positioned behind the ribs, muscle, skin, and fur when the animal was laid on its back for imaging. The lungs and the heart were located on the dorsal side of the tubes. Finally, the muscle/rib flaps were closed and stapled to the muscle surrounding the spinal column. The muscle was then covered with skin/fur, which was also stapled into place. During the

course of the experiment, the positioning of other fluorescent tubes (Figure 2) was performed by reversing the closing process, switching tubes, and reclosing.

#### Generation of Orthotopic Xenografts

SCID mice were maintained and animal experiments were performed under National Institutes of Health and institutional guidelines established for the Animal Core Facility at Johns Hopkins University. MDA-MB-231-tdTomato breast cancer cells ( $2 \times 10^6$ ) in sterile PBS (100  $\mu\text{l}$ ) were injected into the thoracic mammary fat pads of 8-week-old anesthetized mice. Tumor growth was measured weekly, and volumes ( $\text{mm}^3$ ) were calculated as:  $\text{volume} = 0.524d_1d_2d_3$ , where  $d_1$ ,  $d_2$ , and  $d_3$  are the diameters of each of the three axes of the roughly ellipsoid-shaped tumors. Animal weights were also monitored weekly.

#### Longitudinal Fluorescence Optical Imaging of Live Mice and Image Processing

Live animal fluorescence optical imaging was performed using the Xenogen system within the Johns Hopkins University Molecular Imaging Center. Imaging parameters were selected and implemented through the instrument, Living Image 2.5 software. A number of different fluorophore excitation and emission filter sets were used, as indicated in the Results section. Bright field photographs were obtained for each imaging time. The merged bright field photograph and fluorescent images were generated using Adobe PhotoShop software (San Jose, CA). The reported fluorescence images are real-time unprocessed images, unless stated otherwise.

#### Postmortem Tissue Preparation

Mice were sacrificed with an overdose of anesthetic, followed by cervical dislocation. Tissues were fixed in formalin for paraffin embedding and for hematoxylin and eosin (H&E) staining. Pieces of lungs were also placed in 20% sucrose–PBS, immersed in Tissue-Tek OCT compound (Sakura Finetek, Inc., Torrance, CA) 24 hours later, and then immediately frozen in liquid nitrogen. Cryostat slides were prepared with a Microm HM550 (Richard-Allen Scientific, Kalamazoo, MI) instrument. Serial sections of 5  $\mu\text{m}$  each were cut and fixed with 0.38% paraformaldehyde–90% methanol in PBS (pH 7.4). One section was H&E-stained, and consecutive sections were stained with DAPI (Sigma, St. Louis, MO). The methanol-based fixative was prepared immediately before use to avoid precipitation.

#### Fluorescent Microscopy

Fluorescent and H&E photomicrographs of tissue samples were captured on a Nikon ECLIPSE 80i upright microscope (Nikon, Melville, NY), whereas fluorescent and phase-contrast photomicrographs of cell cultures were captured on a Nikon ECLIPSE TS100 inverted microscope. The microscopes were equipped with a charge-coupled device CoolSNAP ES (Roper Scientific, Tucson, AZ) camera, B 2E/C DAPI or B E/C FITC and Y 2E/C Texas red fluorescent filter cubes, and a Micro\*Color Liquid Crystal Tunable RGB Filter (Cambridge Research and Instrumentation, Inc.).

The Micro\*Color RGB filter allowed for the direct collection of color images from H&E-stained slides. Fluorescence and phase-contrast images were processed with Image Pro Plus 5.1 (Media Cybernetics, Inc., Silver Spring, MD) software, whereas H&E images were processed with QED capture (Media Cybernetics, Inc.) software.

## Results

### Detection of Orange-Red, Far-Red, and GFP Expression in Tissue Culture Cells with the Xenogen System

To extend the application of fluorescent protein-based optical imaging beyond superficial lesions in animals, the engineering of fluorescent proteins has focused on the development of fluorophores with orange-red to far-red ( $\lambda_{\text{emission}} = 580\text{--}650$  nm) fluorescence characteristics [1, 8–10]. Such fluorescent proteins may circumvent the attenuation of the signal within animal tissues, which occurs at wavelengths below 600 nm [2, 11]. For example, the evaluation of green *versus* red bioluminescence in the Xenogen system indicated that green bioluminescence is essentially undetectable in animal tissues, whereas red bioluminescence retained 40% to 50% of its *in vitro* intensity when detection was at wavelengths above 600 nm [12]. However, these data are in contrast to several studies where GFP fluorescence has been reported to be detectable in lesions other than superficial lesions in nude mice [13–17]. Thus, it was important to establish whether GFP fluorescence could be intense enough to be detected in SCID mice using the Xenogen system. To test GFP ( $\lambda_{\text{emission}} = 510$  nm) [18], as well as the three newly generated proteins tdTomato ( $\lambda_{\text{emission}} = 581$  nm), mCherry ( $\lambda_{\text{emission}} = 610$  nm), and mPlum ( $\lambda_{\text{emission}} = 649$  nm) [1, 8], for their suitability as *in vivo* optical imaging reporters, we initially carried out a transient expression of these proteins in MCF-7 breast cancer cells. As shown on the *upper panels* of Figure 1A, bright fluorescent photomicrographs were obtained for each protein expressed in MCF-7 cells that indicated similar transfection efficiency in all four cases. In an attempt to eliminate human bias with respect to the evaluation of the most intense fluorescence, the camera was set on autoexposure. Under these conditions, tdTomato exhibited the highest fluorescent intensity (25 milliseconds of exposure) compared to mCherry (60 milliseconds of exposure), GFP (125 milliseconds of exposure), and mPlum (930 milliseconds of exposure) (Figure 1A, *upper panels*). As shown on the *upper right panel* of Figure 1A, even at 200 milliseconds, no autofluorescence was detected in MCF-7 cells transfected with an empty vector when either filter cube [green filter (GF) or red filter (RF)] was in place. These results are in concordance with the data reported by Shaner et al. [1] and Wang et al. [8], which showed that tdTomato had the brightest fluorescence among the proteins described at that time, including GFP. Subsequently, we determined the ability of the Xenogen system to detect the fluorescence of these transient expressions using broad bandwidth filter sets, which is  $\lambda_{\text{excitation}} = 500\text{--}550$  nm and  $\lambda_{\text{emission}} = 575\text{--}650$  nm for DsRed, and  $\lambda_{\text{excitation}} = 445\text{--}$

490 nm and  $\lambda_{\text{emission}} = 515\text{--}575$  nm for GFP. As shown on the *lower left panel* of Figure 1A, with the DsRed filter set, tdTomato fluorescence was more intense than mCherry fluorescence, and mPlum fluorescence was not detectable. The bar spectrum shown on the right of the six-well plate indicates that the range of fluxes in this case was roughly 200 to 800 million photons/sec/cm<sup>2</sup>/sr. As depicted on the *lower right panel* of Figure 1A, with the GFP filter set, GFP fluorescence intensities were, on average, five-fold to eight-fold lower than those of tdTomato, as indicated by their range of roughly 60 to 150 million photons/sec/cm<sup>2</sup>/sr. Importantly, only one six-well plate was used in this experiment; thus, GFP fluorescence was not detected with the DsRed filter set, and no red fluorescence was detected with the GFP filter set. In addition, no autofluorescence was detected in MCF-7 cells transfected with the empty vector.

Subsequently, we used the spectral scanning capabilities of the Xenogen system, which uses 20-nm bandwidth emission filters, to determine the intensities of red fluorescent proteins at emission wavelength maximums centered on 600, 620, 640, 660, 680, or 700 nm (Figure 1B), with excitations using the DsRed filter. These intensities were compared to the default broad bandwidth emission filter of the DsRed filter set (Figure 1A, *lower left panel*). From these experiments, tdTomato gave the highest signal intensities when using the DsRed filter set (Figure 1A), which was equal to a 580-nm emission filter (not shown). tdTomato intensities at 600 nm approximately equaled those at 620 nm and were about one third of the DsRed filter set at the maximum at 640 and 660 nm; tdTomato intensities dropped to about one fifth of the DsRed filter set at maximum; at 680 and 700 nm, tdTomato was only one tenth as intense. Although mPlum, which emits in the far-red range (maximum at 649 nm), would be expected to have maximum penetration in *in vivo* studies [7, 11], its low quantum yield [8] and perhaps low extinction coefficient (the latter has not been reported) made it difficult to detect even when using 640- or 660-nm emission filters. Thus, spectral scanning with the Xenogen system confirmed the low intensity of mPlum. However, mCherry, which is brighter than mPlum, with an emission maximum at 610 nm, was detectable throughout the range of wavelengths tested, but was not as bright as tdTomato, and its brightness decreased as a function of increasing wavelength. Contrary to this result, it was anticipated that mCherry should have had its highest intensities in the range of 600 to 620 nm, and perhaps should have been as intense as tdTomato at these wavelengths, which encompass its emission maximum. Instead, the quantum yield for tdTomato that is more than double that of mCherry [1], along with brightness that is three-fold to five-fold higher than that of mCherry (as shown in this study and in Shaner et al. [1]), indicated that tdTomato would be the best available red fluorescence candidate for testing as an *in vivo* fluorescent protein reporter.

Following the characterization of these fluorescent proteins, we stably overexpressed the tdTomato protein (using an EF-1 $\alpha$ -based expression vector) in the MDA-MB-231 cell line, which is an established mouse model of metastatic

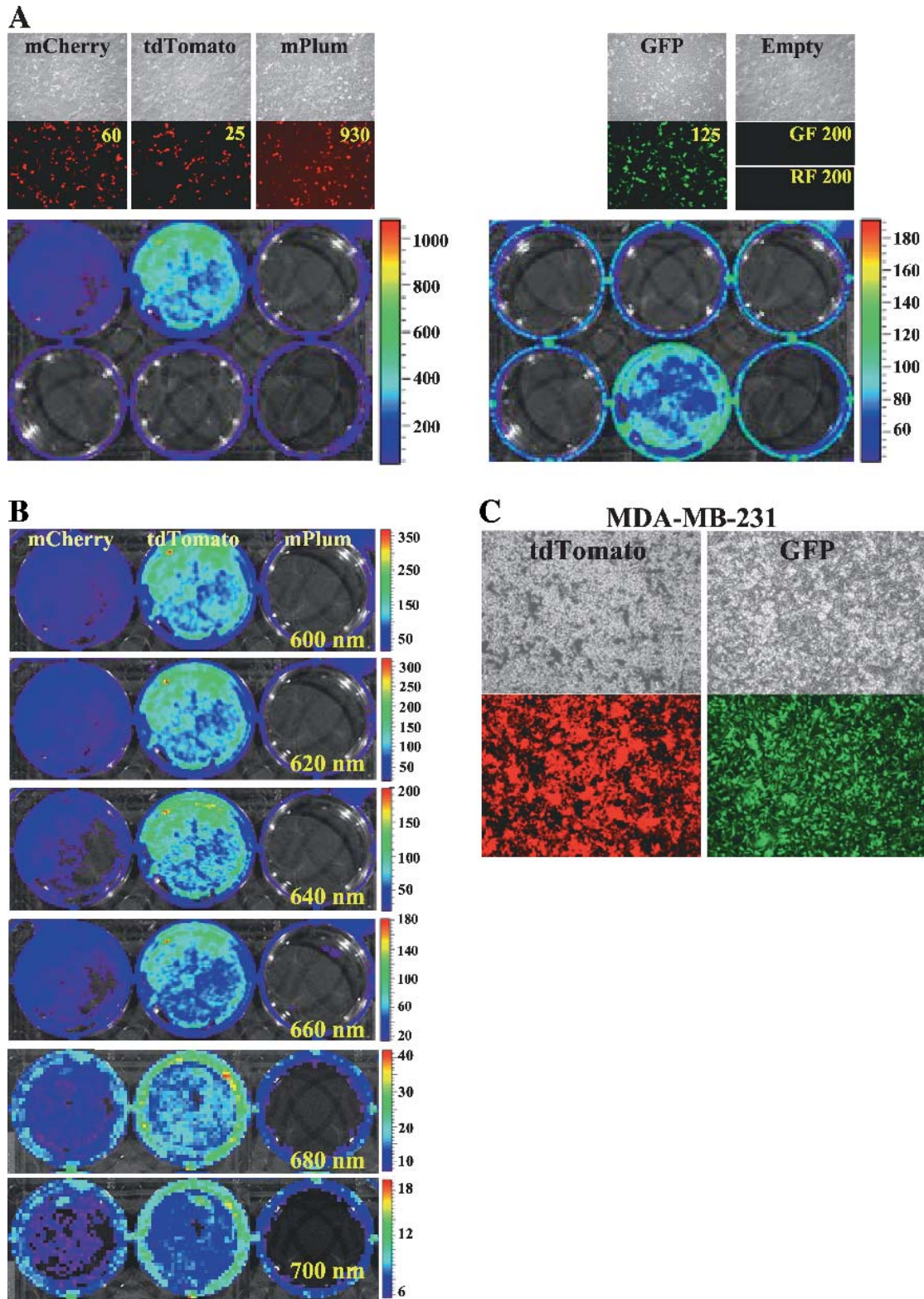


**Figure 1.** Evaluation of the fluorescence intensity of three red fluorescent proteins and GFP when expressed in breast cancer cells with the Xenogen system. Shown on the upper panels of (A) are phase-contrast and corresponding fluorescence images of MCF-7 breast cancer cells transiently expressing mCherry, tdTomato, mPlum, and GFP or the empty vector. The numbers on the upper right corner of the fluorescent images are autoexposure times (in milliseconds) determined by the camera software. No autofluorescence was seen with either the GF cube or the RF cube with a 200-millisecond exposure of the MCF-7 cells transfected with the empty vector. The lower panels of (A) show Xenogen system images of the identical plate of cells shown on the upper panels of (A). False-color overlays represent the spectrum of photon radiance or flux (i.e., photons/sec/cm<sup>2</sup>/sr of the imaged surface), radiating into a solid angle of 1 sr (Xenogen Living Image 2.5 manual). (The bar spectrum on the right of each image of the six-well plate is expressed in photons/sec/cm<sup>2</sup>/sr × 10<sup>6</sup>.) (B) Spectral scanning of red fluorescent proteins using the DsRed excitation filter and the 20-nm bandwidth emission filters centered at 600, 620, 640, 660, 680, and 700 nm, as indicated on the lower right of each scan. (The bar spectrum on the right of each scan is expressed as photons/sec/cm<sup>2</sup>/sr × 10<sup>6</sup>.) (C) Phase-contrast and corresponding fluorescence image of MDA-MB-231 breast cancer cells that stably express tdTomato fluorescence protein and GFP. A uniform cell population with all cells fluorescing bright orange-red or green was observed. All fluorescence and phase-contrast photomicrographs were acquired at ×10 magnification on a Nikon ECLIPSE TS100 inverted microscope equipped with a CoolSNAP ES camera, and Texas red and FITC fluorescence filter cubes. Autoexposure times were determined by Image Pro Plus 5.1.

breast cancer [19,20]. The stable expression of tdTomato in MDA-MB-231 cells was generated without antibiotic selection to maintain cellular homogeneity within the animals (Figure 1C). We also obtained stable MDA-MB-231 cells stably expressing GFP (Figure 1C) for comparison studies in our mouse cadaver phantom.

#### Mouse Cadaver Phantom

As noted above, contradictory reports about the detection of GFP fluorescence in mouse studies indicated that we needed to determine if there would be any advantage to using tdTomato over GFP in our optical imaging study. Thus, a SCID mouse cadaver phantom model system (as described in the Materials and Methods section), which is similar to a recently reported mouse cadaver phantom [21], was developed. The *upper left panels* of Figure 2A indicate that tubes packed with either stable MDA-MB-231-tdTomato cells ( $100 \times 10^6$ ) or stable MDA-MB-231-GFP cells ( $100 \times 10^6$ ) remained highly fluorescent after cell processing. Below the fluorescent photomicrographs are photographs and corresponding false-color overlays of these tubes that were produced in the Xenogen system. In both cases, the Xenogen system easily detected (exposure time, 0.01 second) GFP, as seen on the upper right false-color tube image, and tdTomato, as seen on the lower left false-color tube image. As described above for the transient expression experiments seen here, red fluorescence was not detected with the use of the GFP filter set for GFP imaging, and GFP was not detected with the use of the DsRed filter set for tdTomato imaging. The tubes were then positioned on the internal ventral side of the rib cage. As seen on the mouse false-color overlay photographs of Figure 2A, with the regions of interest encircled, only tdTomato fluorescence was detected with these 1-second exposures. Figure 2B shows similar results; however, in this case, the number of MDA-MB-231-tdTomato cells was  $45 \times 10^6$ , whereas the number of MDA-MB-231-GFP cells was the same. As seen on the false-color overlay photographs of the tubes before implantation on the *left* of Figure 2B, the cells remained easily detectable (exposure time, 0.01 second) when imaged outside the animal. As seen on the mouse false-color overlay photographs of Figure 2B, with the regions of interest were encircled for clarity, only the tdTomato fluorescence was detected when these tubes were placed within the rib cage. The *left* and *central panels* of Figure 2C show unprocessed fluorescence images after a 2.5-second exposure time, which were taken during a series of time exposure trials of implanted tubes imaged in Figure 2, A and B, respectively. This autofluorescence from the fur of the SCID mouse completely saturated the sensitive optics of the Xenogen system and thus obliterated the imaging. Based on this result, the mouse images shown in Figure 2, A and B, were obtained with 1-second exposure. This autofluorescence was largely eliminated when imaging tdTomato fluorescence with the 620-nm emission filter rather than with the DsRed emission filter. This is shown on the unprocessed fluorescence image on the *right panel* of Figure 2C, where the *arrow* points to fluorescence from the implant. Moreover, in this case, the implanted tube contained only  $9.25 \times 10^6$

MDA-MB-213-tdTomato cells. The sensitivity of the optics of the Xenogen system is underscored in Figure 2D, where fluorescence (with a 620-nm emission filter) from the implanted  $9.25 \times 10^6$  MDA-MB-213-tdTomato cells was detected with only a 0.01-second exposure time, as indicated within the encircled region of interest of the false-color overlay photograph (Figure 2D, *left panel*). The *central panel* of Figure 2D shows the unprocessed fluorescence image where no apparent fluorescence is seen. However, the faint fluorescence from the implant is visible when the fluorescence image is enhanced with PhotoShop, as shown by the *arrow* on the *right panel* of Figure 2D. As the bar spectrum below the false-color overlay indicates, the camera detected billions of photons per second per square centimeter, and it is this high signal intensity that allowed for the reliable construction of the overlay.

The results shown in Figures 1 and 2 indicate that, despite the *in vitro* detection of GFP fluorescence, this GFP signal was undetectable in our mouse cadaver phantom. Of the red fluorescent proteins tested, the intensity of tdTomato at emission wavelengths above 600 nm was much greater than those of mCherry and mPlum. In addition, imaging at wavelengths of  $\geq 620$  nm, where autofluorescence was minimized, greatly increased the penetration of fluorescence signals into the tissues.

#### Longitudinal Optical Imaging of Metastatic Progression in a Breast Cancer Xenograft Model System

Tumor xenografts were generated by injecting  $2 \times 10^6$  MDA-MB-231-tdTomato cells into the first or the second thoracic mammary fat pad of six SCID mice. The photographs shown in Figure 3A (*upper panel*) indicate that at 2 weeks postinjection, barely palpable and invisible lesions could be detected as a single bright spot of fluorescence at each injection site, with an exposure time of only 0.25 second. The localization of the fluorescence at the injection site was verified by the digital merging of the upper and middle images, as shown on the *lowest panel* of Figure 3A. Thus, the combination of the intense fluorescence of tdTomato and the sensitivity of the instrumentation enabled the imaging of extremely small MDA-MB-231-tdTomato tumor burdens with high specificity. The continued tracking of tumor growth indicated that tumors measuring about  $45 \text{ mm}^3$  were easily detected (Figure 3B, *top panel*). Moreover, we found that even small primary lesions ( $82 \text{ mm}^3$ ) could give rise to metastatic lesions (Figure 3B, *lower panel*). The observed metastatic lesion on a contralateral mammary fat pad (*arrow*) was visible with only a 1-second exposure time and was greatly intensified at a 5-second exposure time (Figure 3B, *inset*). The detection of a metastatic lesion on the contralateral mammary fat pad has not been previously reported for this xenograft model. It is possible that lower detection limits of previous methods may have contributed to the inability to track such small lesions. Importantly, the use of this optical imaging probe, with the resulting detection of a mammary fat pad lesion, validates the use of MDA-MB-231 cells in animal models, which can mimic the progression of human breast cancer metastasis [22,23].

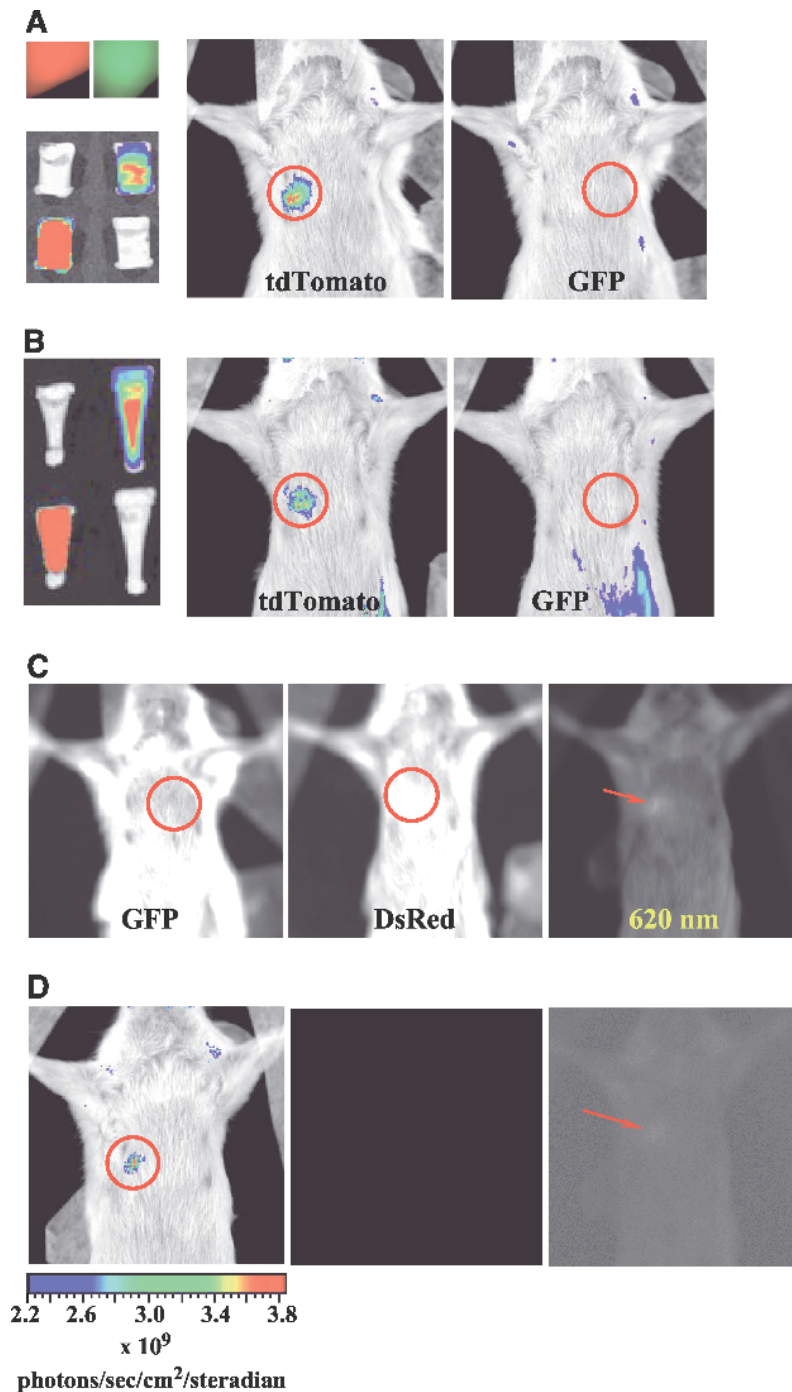


**Figure 2.** Evaluation of the detection of tdTomato and GFP fluorescence in the mouse cadaver phantom with the Xenogen system. The upper left panel of (A) shows fluorescence from tubes packed with  $100 \times 10^6$  MDA-MB-231-tdTomato-expressing (red) or MDA-MB-231-GFP-expressing (green) cells. Below these are false-color overlay images (exposure time, 0.01 second) acquired with the Xenogen system using either the GFP filter set or the DsRed filter set. The white tubes on these images indicate that tdTomato did not fluoresce when GFP was being imaged and that GFP did not fluoresce when tdTomato was being imaged. The mouse false-color overlay images (regions of interest were encircled; exposure time, 1 second) at the center and on the right of (A) show that the Xenogen system only detected tdTomato fluorescence from implanted tubes. (B) Similar results were found only in the number of tdTomato cells used ( $45 \times 10^6$ ), whereas the number of GFP-expressing cells remained the same. Implanted tubes are shown on the left, where it is seen that red and green fluorescence were easily detected (exposure time, 0.01 second). (C) Autofluorescence from the fur of the SCID mouse depends on the emission wavelength filter used, as indicated on the bottom of each image. All three are unprocessed fluorescent images with a 2.5-second exposure time. Tube implants were those shown in (A) (left image) and (B) (center image), and in a tube containing  $9.25 \times 10^6$  tdTomato-expressing cells (right image). Regions of interest are encircled in the first two cases. The left and center show the very intense fur autofluorescence that masks the detection of implanted fluorescence signals. The right image indicates that the use of a 620-nm emission filter allowed the lowest number of implanted tdTomato cells to be detected (fluorescent signal indicated by an arrow) above fur autofluorescence. (D) Excellent sensitivity of the Xenogen system. The false-color overlay on the left, with the region of interest encircled, shows the detection of the fluorescence signal of the  $9.25 \times 10^6$  tdTomato cell implant using a 0.01-second exposure and a 620-nm emission filter. (The bar spectrum below the image is expressed as photons/sec/cm<sup>2</sup>/sr  $\times 10^9$ .) The faint fluorescence from the implant has been made visible by enhancing the central image with PhotoShop, as indicated by the arrow on the image on the right.

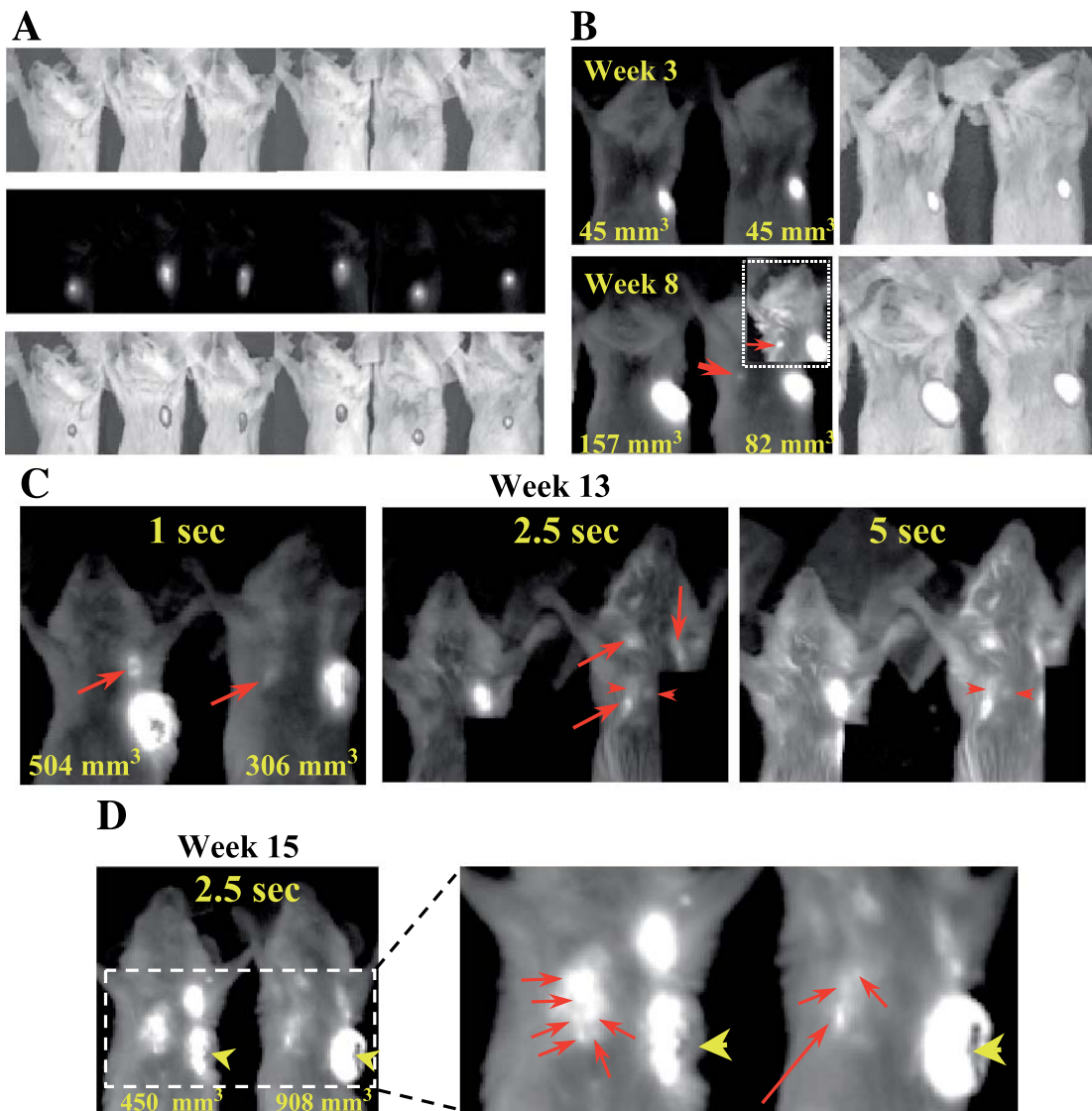


**Figure 3.** Fluorescence optical tracking of the metastatic progression of MDA-MB-231-tdTomato in SCID mice. (A) Fluorescent images at 2 weeks postinjection of MDA-MB-231-tdTomato cells in either the first or the second mammary fat pad (bottom photographs). As depicted, the barely palpable invisible tumors (top photographs) were detected (center fluorescence images) with only a 0.25-second exposure time in the Xenogen system imager. Bright fluorescence spots on center images perfectly matched the sites of injection (bottom merged photographs). (B) Fluorescence and merged photographs of two representative mice at 3 weeks (top panel) and 8 weeks (bottom panel) post-MDA-MB-231-tdTomato cell injection. Caliper-measured tumor volumes are given at the bottom of the fluorescent images. Small tumors were easily imaged at 3 weeks and by 8 weeks, a metastatic lesion at a contralateral mammary fat pad had become visible with just a 1-second exposure time. The inset shows the image of the identical area after a 5-second exposure time. In addition, at 8 weeks, tumor sizes visualized with fluorescence imaging were in agreement with those measured with calipers; that is, the larger of the two tumors (157 mm<sup>3</sup>) is shown by fluorescence to be twice as large as the smaller one (82 mm<sup>3</sup>). (C) Fluorescent images of the same mice at 13 weeks post-MDA-MB-231-tdTomato cell injections with 1-, 2.5-, and 5-second exposure times. Nonfluorescent necrotic areas of the tumor are visible as hypointense patches in otherwise intensely fluorescent tumors. The arrows in the 1-second exposure images point to metastases to the axillary lymph node and contralateral mammary fat pad (dim images) of the mouse on the right and on the left, respectively. The primary tumor xenografts for the 2.5- and 5-second exposure times were covered with a blocking sheet to decrease bleedover fluorescence to nearby organs. Arrows in the 2.5-second exposure image clearly identify the contralateral mammary fat pad, as well as lymph nodes, in the other animal; arrowheads point out the faint detection of lung region metastasis. As shown, all metastases are easily identifiable as very bright areas of fluorescence on 5-second exposure images. (D) A fluorescent image after a 2.5-second exposure of the same two mice at 15 weeks after tumor cell injections. Tumor fluorescence shows that the tumor in the mouse to the left has regressed whereas the tumor on the mouse to the right has grown rapidly from Week 13. Caliper-measured volumes agree with fluorescence. Enlargement of the region of interest shows that the very large area of bright fluorescence in the pleural tissue/lung region is made up of clusters of smaller fluorescent masses (short arrows). Contralateral mammary fat pad metastasis is still apparent (long arrow). The central necrotic portions of the tumors appear as dark regions (arrowheads).

Longitudinal *in vivo* imaging of these tumor xenografts (week 13) showed hypointense patches within the fluorescent region encompassing the tumors (Figure 3C). These hypointense areas were due to necrotic tumor tissues that were no longer fluorescent. Concurrently, the contralateral

breast lesion remained visible (arrow), and additional axillary lymph node metastases were visible as two bright spots above and to the right of the tumor (arrow). Subsequent increases of exposure time greatly enhanced the fluorescence of these metastatic lesions, as well as the faint

fluorescence of pleural tissues/lung metastases (Figure 3C, *arrowheads, middle and right photos*). This increased sensitivity allowed for the unambiguous determination of the relative sizes and locations of the metastatic lesions. On week 15, metastatic lesions within the rib cage were visible with a 2.5-second exposure (Figure 3D). In addition, the nodular characteristic of these metastatic lesions was apparent following image magnification (Figure 3D, *lower portion*). One could also observe a contralateral mammary fat pad metastatic lesion (*long arrow*), individual or small clusters of nodules in the lungs (*short arrows*), and necrotic regions of intensely fluorescent tumors (*arrowheads*). Importantly, postmortem lung tissues confirmed the nodular character of lung and pleural tissue metastases (Figure 4, *left panel*). It was also observed that differences in the growth rates of primary tumors (Figure 4, *right panel*) appeared to be independent of the general metastatic process (Figure 4, *left panel*). Taken together, these results indicate that, throughout the study, the expression of tdTomato remained high, and its intense fluorescence enabled the *in vivo* optical tracking of different metastatic lesions.

#### Facility Identification of Micrometastases by Fluorescence Microscopy as Verified by Histologic Analyses

To verify the ability of this fluorescence technique to detect very small metastatic lesions, serial cryostat sections of one of six lung tissues (Figure 4A) were examined using fluorescence microscopy. One of each pair of consecutive fixed sections was stained with H&E, and the other was stained with DAPI (nuclear stain). Three small lung metastatic lesions were selected as representative examples of the ability to detect such lesions with fluorescent microscopy (Figure 5A). In each case, H&E staining (Figure 5A, *left panels*) was compared to the fluorescent detection (Figure 5A, *right panels*) of consecutive serial sections. The region with the greatest cancer cell burden was easily detected by fluorescent microscopy at  $\times 10$  magnification (Figure 5A, *top right panel*). Bright fluorescent orange-red cells were easily detected at two other metastatic sites (Figure 5A, *middle right*

and *bottom right panels*). The fluorescent images from the site with the fewest cancer cells (Figure 5A, *bottom panels*) indicated that the fluorescent detection of a small number of cancer cells was feasible.

H&E staining of contralateral mammary fat pad tissues confirmed the presence of tumor cells (Figure 5B). As shown in Figure 5B, tumor cells (*asterisk*) have invaded the mammary fat pad tissue. In addition, from H&E staining, it is apparent that a contralateral (relative to the tumor) axillary lymph node and the axillary lymph node from above a tumor were totally obliterated by invading MDA-MB-231-tdTomato breast cancer cells (Figure 5, C and D, *asterisks*). In both cases, only tumor cells surrounded by some necrotic (hematoxylin-negative) regions were present. Three of six animals showed lymph node involvement, and one of these had metastases in both axillary lymph nodes.

#### Increased Depth of Detection by Imaging at 620 and 660 nm Followed By 3-D Reconstruction

An important consideration in optical imaging is the depth from which the fluorescent signals are detectable. Tumors just beneath the skin, in nude mice and in a melanoma model in SCID mice, have been shown to be optically detectable, using a GFP reporter-based imaging approach [5,24–26]. The imaging of the liver, lungs, or gastrointestinal track in live nude mice with GFP as the reporter has also been reported [14,17]. However, tissue absorption/autofluorescence is a major concern in GFP-based live animal imaging due to imaging in the blue/green region (as shown here; see Doubrovin et al. [2]). Thus, the detection of GFP within internal organs of SCID mice, such as in the lungs and liver, has been limited to postmortem analyses [5,27]. Recently, red fluorescent protein (DsRed)-based fluorescence optical imaging in visceral organs in live nude mice has been reported [6,28]. In our study, the tdTomato fluorescence signal was detectable from within the rib cage, as shown in Figure 3. In an attempt to obtain a first approximation of the depth from which fluorescence was emanating, we applied the 3-D reconstruction program of the Xenogen system. The sagittal and transaxial

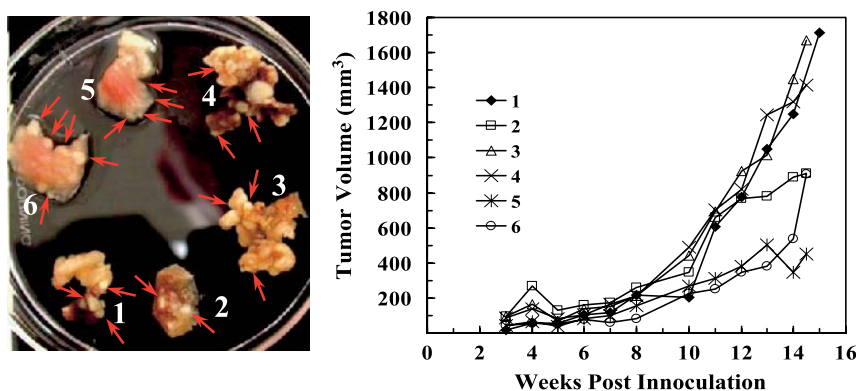


**Figure 4.** The incidence of lung metastases is independent of primary tumor growth rate. Left photograph: Gross morphology of lung metastasis following necropsy, which confirmed the nodular character of the lung and pleural tissue metastases observed during real-time imaging. Lung specimens from different mice are indicated by white numbers. Arrows show individual nodule locations in the respective lungs. The graph on the right shows tumor growth curves plotted as volume ( $\text{mm}^3$ ) against time postinoculation (weeks) for each mouse, as indicated by separate symbols. The images presented in Figure 2 were from two mice with the slowest-growing tumors, which indicates that primary tumor growth rate did not hinder metastatic progression.

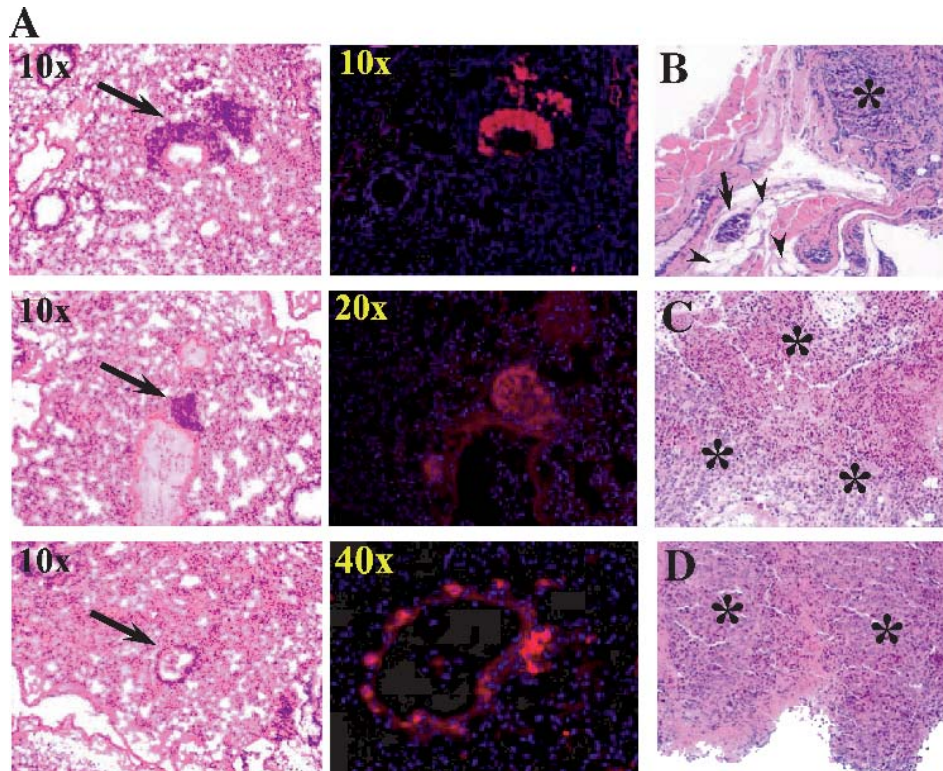


**Figure 5.** Histologic confirmation of metastatic lesions formed by MDA-MD-231-tdTomato cells injected into the mammary fat pad of SCID mice. (A) Three representative examples of microscopic metastatic invasions to the lung. These lesions were identified using H&E staining (left photographs) and in consecutive sections with fluorescent microscopy (right fluorescent photomicrographs). As demonstrated by increasing magnification, the sensitivity of fluorescence imaging decreased with lower tumor burden. However, fluorescent microscopy facilitated the identification of low numbers of fluorescent tumor cells by eliminating the need to score for specific tumor markers. (B) H&E staining of a section of the contralateral mammary fat pad with metastatic invasion. The asterisk indicates tumor cells adjacent to ductal structures (arrow), as well as adipose tissues (arrowheads). (C and D) H&E staining of representative axillary lymph node sections from lymph nodes excised from above a tumor (C) or contralateral to the tumor (D). It can be seen that tumor cell invasion was extensive (asterisks) and has completely abolished lymph node structure.

sections shown in Figure W1 indicated that the dorsal–ventral depth of the animal was 2.5 cm and that the center of the fluorescent signal from within the rib cage cavity was at a depth of roughly 1 cm. The 3-D reconstruction program has been designed for use with bioluminescence data and does not account for fluorescence excitation signal attenuation by absorption and scatter. However, because the emission wavelengths used (620 and 660 nm) are very similarly used during luciferase-based bioluminescence imaging [7] and because the photon densities and source intensities are similar to those observed with bioluminescence imaging, we have been advised that these results likely represent a good first estimate of tissue penetration (technical support staff at Xenogen Corp., personnel communication).

## Discussion

Endogenously expressed fluorescence protein–based optical imaging has the advantage of requiring neither a substrate (as bioluminescence does) nor a targeted fluorescence probe. The need to administer such reagents complicates the issue of uniform delivery to all tumor cells, which may produce false-negative images. In addition, the temporal sequence of the imaging event following substrate/probe injection must be ascertained [29,30]. Furthermore,

luciferase-based bioluminescence requires adenosine triphosphate, which precludes its use to only metabolizing cells. Finally, a microscopic bioluminescent evaluation equivalent to the microscopic fluorescence information presented in Figure 4 is not feasible. Nevertheless, when adequate substrate concentration is attained, bioluminescence provides sensitive detection with high signal-to-noise ratios due to a lack of autoluminescence [31] and has often been successfully used for the optical imaging of SCID mice (e.g., see Minn et al. [32]).

The usefulness of light-based diagnostic techniques had been recognized as early as the mid 1920s when transillumination of the human breast with an intense light source revealed inner abnormalities, such as chronic mastitis, tumor, and hematoma [33]. This simple approach of passing light through a relatively translucent or transparent tissue as a means of “imaging” inner structures even in the absence of a fluorescence reporter may, in part, explain the divergent reports on the use of GFP as a reporter in animal optical imaging studies. Albeit numerous papers have reported the detection of GFP in visceral organs of live nude mice, GFP has been considerably more difficult to detect or has been virtually undetectable in SCID mice. This is because GFP has a wavelength excitation maximum of ~490 nm and a wavelength emission maximum of ~510 nm [18], which are both

within the wavelength region where animal tissue has high absorption/autofluorescence [7,11,12,31]. Nonetheless, several investigations using GFP have proven the simplicity of the fluorescent protein–based optical imaging of cancer cells in live animals [5,13–17,24–28] and its sensitivity, which potentially allows for the detection of a single fluorescent cell.

Our evaluation of the red fluorescent protein–based optical imaging of SCID mice has demonstrated similar results, as well as an increase in sensitivity, as indicated by our mouse cadaver phantom where GFP fluorescence was undetectable. This increase in sensitivity is due to tdTomato's intense fluorescence, the use of emission detection at 620 to 660 nm, and the sensitivity of the optics of the Xenogen system. In many respects, the difficulties experienced while attempting to obtain fluorescent signal penetration in SCID mice (where fur is an additional impedance to fluorescence signal penetration) are at the core of challenges presented by the present limitations of using fluorescence protein–based optical imaging in live animals. Thus, future studies will attempt to improve the use of tdTomato-based or mCherry-based imaging. First, replacing the default DsRed excitation filter with those that encompass the excitation range of these proteins (i.e., with a bandwidth of 520–590 nm for tdTomato and of 550–610 nm for mCherry) should increase the efficiency of the *in vivo* excitation of these proteins. Second, a modification of mCherry in a manner that results in a brighter alternative while, at the same time, maintaining its 610-nm emission maximum may then extend the use of this protein to *in vivo* studies. Finally, the use of an image capture analysis program that will take into account the attenuation of the excitation signal by absorption and scatter and its incorporation into 3-D reconstruction analyses should be encouraged. Despite the needed improvements, this study indicates the feasibility of using tdTomato and similar proteins for the optical tracking of a variety of cell types in studies aimed at acquiring a better understanding of many crucial biological processes.

### Acknowledgements

Special thanks to Roger Tsien for supplying tdTomato cDNA, Carrie Bhang for help with plasmid cloning, and Kathleen Gabrielson (veterinary pathologist) for interpreting histology slides. We thank Dmitri Artemov, Arvind Pathak, Farhad Vesuna, and Zaver Bhujwalla for helpful comments on the manuscript. We also thank Baasil Okollie, Steven McNutt, and Michele Doucet for technical assistance.

### References

- Shaner NC, Campbell RE, Steinbach PA, Giepmans BN, Palmer AE, and Tsien RY (2004). Improved monomeric red, orange and yellow fluorescent proteins derived from *Discosoma* sp. red fluorescent protein. *Nat Biotechnol* **22**, 1567–1572.
- Dobrovinn M, Serganova I, Mayer-Kuckuk P, Ponomarev V, and Blasberg RG (2004). Multimodality *in vivo* molecular–genetic imaging. *Bioconjug Chem* **15**, 1376–1388.
- Chudakov DM, Lukyanov S, and Lukyanov KA (2005). Fluorescent proteins as a toolkit for *in vivo* imaging. *Trends Biotechnol* **23**, 605–613.
- Kanematsu A, Yamamoto S, Iwai-Kanai E, Kanatani I, Imamura M, Adam RM, Tabata Y, and Ogawa O (2005). Induction of smooth muscle cell–like phenotype in marrow-derived cells among regenerating urinary bladder smooth muscle cells. *Am J Pathol* **166**, 565–573.
- Henriksson KC, Almgren MAE, Thurlow R, Varki NM, and Chang CL (2004). A fluorescent orthotopic mouse model for reliable measurement and genetic modulation of human neuroblastoma metastasis. *Clin Exp Metastasis* **21**, 563–570.
- Bouvet M, Spornyak J, Katz MH, Mazurchuk RV, Takimoto S, Bernacki R, Rustum YM, Moossa AR, and Hoffman RM (2005). High correlation of whole-body red fluorescent protein imaging and magnetic resonance imaging on an orthotopic model of pancreatic cancer. *Cancer Res* **65**, 9829–9833.
- Rice BW, Cable MD, and Nelson MB (2001). *In vivo* imaging of light-emitting probes. *J Biomed Opt* **6**, 432–440.
- Wang L, Jackson WC, Steinbach PA, and Tsien RY (2004). Evolution of new nonantibody proteins via iterative somatic hypermutation. *Proc Natl Acad Sci USA* **101**, 16745–16749.
- Gurskaya NG, Fradkov AF, Terskikh A, Matz MV, Labas YA, Martynov VI, Yanushevich YG, Lukyanov KA, and Lukyanov SA (2001). GFP-like chromoproteins as a source of far-red fluorescent proteins. *FEBS Lett* **507**, 16–20.
- Wiedenmann J, Vallone B, Renzi F, Nienhaus K, Ivanchenko S, Rocker C, and Nienhaus GU (2005). Red fluorescent protein eqFP611 and its genetically engineered dimeric variants. *J Biomed Opt* **10**, 14003.
- Weissleder R (2001). A clearer vision for *in vivo* imaging. *Nat Biotechnol* **19**, 316–317.
- Zhao H, Doyle TC, Coquoz O, Kalish F, Rice BW, and Contag CH (2005). Emission spectra of bioluminescent reporters and interaction with mammalian tissue determine the sensitivity of detection *in vivo*. *J Biomed Opt* **10**, 41210.
- Bouvet M, Yang M, Nardin S, Wang X, Jiang P, Baranov E, Moossa AR, and Hoffman RM (2000). Chronologically-specific metastatic targeting of human pancreatic tumors in orthotopic models. *Clin Exp Metastasis* **18**, 213–218.
- Zhao M, Yang M, Baranov E, Wang X, Penman S, Moossa AR, and Hoffman RM (2001). Spatial–temporal imaging of bacterial infection and antibiotic response in intact animals. *Proc Natl Acad Sci USA* **98**, 9814–9818.
- Chaudhuri TR, Mountz JM, Rogers BE, Partridge EE, and Zinn KR (2001). Light-based imaging of green fluorescent protein–positive ovarian cancer xenografts during therapy. *Gynecol Oncol* **82**, 581–589.
- Mocanu JD, Moriyama EH, Chia MC, Li J-H, Yip KW, Huang DP, Bastianutto C, Wilson BC, and Liu F-F (2004). Combined *in vivo* bioluminescence and fluorescence imaging for cancer gene therapy. *Mol Imaging* **3**, 352–355.
- Schmitt CA, Fridman JS, Yang M, Baranov E, Hoffman RM, and Lowe SW (2002). Dissecting p53 tumor suppressor functions *in vivo*. *Cancer Cell* **1**, 289–298.
- Cormack BP, Valdivia RH, and Falkow S (1996). FACS-optimized mutants of the green fluorescent protein (GFP). *Gene* **173**, 33–38.
- Bandyopadhyay A, Zhu Y, Cibull ML, Bao L, Chen C, and Sun L (1999). A soluble transforming growth factor  $\beta$  type III receptor suppresses tumorigenicity and metastasis of human breast cancer. *Cancer Res* **59**, 5041–5046.
- Jenkins DE, Hornig YS, Oei Y, Dusich J, and Purchio T (2005). Bioluminescent human breast cancer cell lines that permit rapid and sensitive *in vivo* detection of mammary tumors and multiple metastases in immune deficient mice. *Breast Cancer Res* **7**, R444–R454.
- Schulz RB, Ripoll J, and Ntziachristos V (2004). Experimental fluorescence tomography of tissues with noncontact measurements. *IEEE Trans Med Imaging* **23**, 492–500.
- Mullen EE, Deutsch M, and Bloomer WD (1997). Salvage radiotherapy for local failures of lumpectomy and breast irradiation. *Radiation Oncol* **42**, 25–29.
- Kirkby-Bott J, Cunnick G, and Kissin MW (2005). T1 G1 NO ER positive breast cancer–adjuvant therapy is needed. *Eur J Surg Oncol* **31**, 369–372.
- Li X, Wang J, An Z, Yang M, Baranov E, Jiang P, Sun F, Moossa AR, and Hoffman RM (2002). Optically imageable metastatic model of human breast cancer. *Clin Exp Metastasis* **19**, 347–350.
- Goodison S, Kawai K, Hihara J, Jiang P, Yang M, Urquidí V, Hoffman RM, and Tarin D (2003). Prolonged dormancy and site-specific growth potential of cancer cells spontaneously disseminated from nonmetastatic breast tumors as revealed by labeling with green fluorescent protein. *Clin Cancer Res* **9**, 3808–3814.
- Mitsiades CS, Mitsiades NS, Bronson RT, Chauhan D, Munshi N, Treon

- SP, Maxwell CA, Pilarski L, Hideshima T, Hoffman RM, et al. (2003). Fluorescence imaging of multiple myeloma cells in a clinically relevant SCID/NOD *in vivo* model: biologic and clinical implications. *Cancer Res* **63**, 6689–6696.
- [27] Maeda H, Segawa T, Kamoto T, Yoshida H, Kakizuka A, Ogawa O, and Takechi Y (2000). Rapid detection of candidate metastatic foci in the orthotopic inoculation model of androgen-sensitive prostate cancer cells introduced with green fluorescent protein. *Prostate* **45**, 335–340.
- [28] Katz MH, Takimoto S, Spivack D, Moossa AR, Hoffman RM, and Bouvet M (2004). An imageable highly metastatic orthotopic red fluorescent protein model of pancreatic cancer. *Clin Exp Metastasis* **21**, 7–12.
- [29] Burgos JS, Rosol M, Moats RA, Khankaldyyan V, Kohn DB, Nelson MD Jr, and Laug WE (2003). Time course of bioluminescent signal in orthotopic and heterotopic brain tumors in nude mice. *BioTechniques* **34**, 1184–1188.
- [30] Ignowski JM and Schaffer DV (2004). Kinetic analysis and modeling firefly luciferase as a quantitative reporter gene in live mammalian cells. *Biotech Bioeng* **86**, 827–834.
- [31] Troy T, Jekic-McMullen D, Sambucetti L, and Rice B (2004). Quantitative comparison of the sensitivity of detection of fluorescent and bioluminescent reporters in animal models. *Mol Imaging* **3**, 9–23.
- [32] Minn AJ, Kang Y, Serganova I, Gupta GP, Giri DD, Doubrovin M, Ponomarev V, Gerald WL, Blasberg R, and Massague J (2005). Distinct organ-specific metastatic potential of individual breast cancer cells and primary tumors. *J Clin Invest* **115**, 44–55.
- [33] Culter M (1929). Transillumination as an aid in the diagnosis of breast lesions. *Surg Gynecol Obstet* **48**, 721–729.

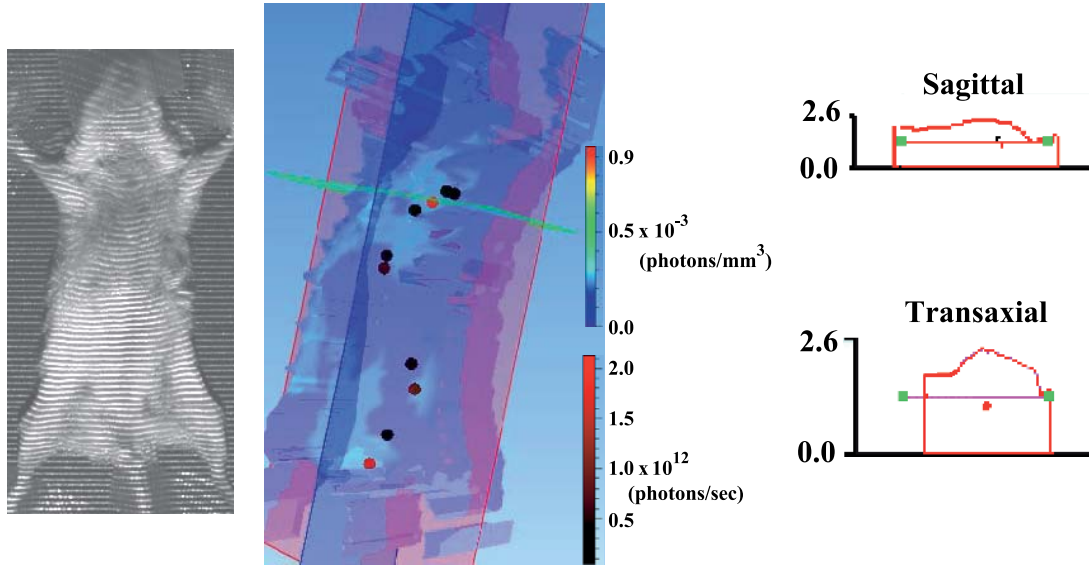


**Figure W1.** Image reconstruction to estimate the penetration depth of the fluorescent signal from the tdTomato protein. The reconstruction is shown on the center panel. The false-colored contour map represents a map of photon densities that have been assigned their coloration based on a multicolored bar spectrum ( $\text{photons}/\text{mm}^3 \times 10^{-3}$ ) shown on the right of the reconstruction. To obtain this map, the program fills a structure image (left panel) with cubic voxels and scores the fluorescence density of each voxel. Red and dark circles within the reconstruction indicate sources of fluorescence that lay on the selected coronal (violet), sagittal (blue), and transaxial (green) planes. As seen from the black-to-red bar spectrum on the lower right of the reconstruction, the intensity of fluorescence from these sources is on the order of  $10^{12}$  photons/sec. The enlarged sagittal and transaxial sections indicate that the dorsal–ventral depth of the animal was about 2.5 cm. The center (red dot) of a fluorescent source from within the rib cage cavity was about halfway through the animal or approximately 1.0 cm from the ventral surface. 3-D reconstructions were performed with the Xenogen Living Imaging 3-D analysis software package (used according to the instruction manual) on images collected on week 15 (with a 2.5-second exposure) and at emission wavelengths of 620 and 660 nm.